

A Discrete Immersed Boundary Method for the numerical simulation of heat transfer in compressible flows

H. Riahi^a, E. Goncalves da Silva^a, M. Meldi^b

^a*Institut Pprime, Department of Fluid Flow, Heat Transfer and Combustion, CNRS - ENSMA - Université de Poitiers, UPR 3346, SP2MI - Téléport, 211 Bd. Marie et Pierre Curie, B.P. 30179 F86962 Futuroscope Chasseneuil Cedex, France*

^b*Arts et Métiers ParisTech, CNRS, Univ. Lille, ONERA, Centrale Lille, UMR 9014-LMFL- Laboratoire de Mécanique des fluides de Lille- Kampé de Fériet, F-59000 Lille, France*

Abstract

In the present study, a discrete forcing Immersed Boundary Method (IBM) is proposed for the numerical simulation of high-speed flow problems including heat exchange. The flow field is governed by the compressible Navier-Stokes equations, which are resolved by using the open source library OpenFOAM. The numerical solver is modified to include source terms in the momentum equation and in the energy equation, which account for the presence of the immersed body. The method is validated on some benchmark test cases dealing with forced convection problems and moving immersed bodies. The results obtained are in very good agreement with data provided in the literature. The method is further assessed by investigating three-dimensional high Mach flows around a heated sphere with different wall temperature. Even for this more complex test case, the method provides an accurate representation of both thermal and velocity fields.

Keywords: immersed boundary method, heat transfer, forced convection, compressible flows, fluid-structure interaction, OpenFOAM.

*Corresponding author, marcello.meldi@ensam.eu

1. Introduction

With the rapid increase of computational resources available in computational centers, the numerical representation of flows around complex configurations of industrial interest is becoming an established reality. A large effort by the scientific community in the last decades has allowed to identify strategies for the numerical investigation of such problems. As a result, new methods studied to solve problematic aspects of the simulations are getting to maturity. Among these, the Immersed Boundary Method (IBM) [1, 2, 3, 4, 5] is an increasing popular tool for the representation of moving bodies. In the IBM, the presence of the immersed body is represented via the inclusion of source terms in the dynamic equations of the physical model. The usage of the IBM allows to naturally exclude problematic aspects of the mesh procedure, such as deformed / stretched mesh elements for the representation of complex geometries. These aspects can result in very large numerical errors, significantly affecting the prediction of the flow features. In addition, IBM can naturally account for the immersed body motion / deformation with almost zero computational resources, excluding expensive re-meshing procedures.

While many different IBM proposals can be found in the literature for purely dynamic effects associated with the immersed body [6, 7, 8, 9, 10, 11] (i.e. focusing on the determination of a source forcing term for the momentum equation) the analysis of heat transfer via IBM is less investigated and mainly dealing with incompressible flow simulation [12, 13, 14]. Recent works on the subject have been proposed by Luo et al. [15, 16] on fixed bodies. Also, simulations of compressible flows in interaction with moving solids are still rare (see for example Qu et al. [17] and Khalili et al. [18]) and very few contributions can be found including the coupling with heat exchange effects [16]. Accounting for heat transfer effects in IBM applications for compressible flows will provide significant advances for a number of relevant high speed applications, such as the flow in aerospace engines. In fact, many features of the flow such as the behavior of the boundary layer of coherent structure organization in turbulent

wakes is affected by thermal phenomena occurring between the flow and the surface of the immersed body. The correct representation of such phenomena is essential for an accurate prediction of heat dissipation in complex mechanical systems.

In the present work, the IBM tool recently developed for integration in the opensource platform *OpenFOAM* [19, 20] is extended to the analysis of heat exchange for compressible flows. To do so, an explicit term is included in the energy equation of the dynamic system. The article is structured as follows. In section 2 numerical details about the dynamic system and the IBM method are provided and the implementation of the IBM method within the numerical solver is detailed. In section 3 the research tool is validated with the analysis of academic test cases. In section 4, a three-dimensional application is analyzed, considering the flow around a heated sphere. In section 5, elements of fluid-structure interaction are discussed via the analysis of an oscillating cylinder. Finally, concluding remarks are drawn in section 6.

2. Numerical ingredients and Immersed Boundary Method

The IBM algorithm developed for heat transfer prediction is here introduced and its analytic derivation is described.

2.1. Governing equations

The starting point is represented by the general Navier–Stokes equations for a compressible fluid:

$$\frac{\partial \rho}{\partial t} + \operatorname{div}(\rho \mathbf{u}) = 0 \quad (1)$$

$$\frac{\partial \rho \mathbf{u}}{\partial t} + \mathbf{div}(\rho \mathbf{u} \otimes \mathbf{u}) = -\mathbf{grad} p + \mathbf{div} \bar{\bar{\tau}} + \mathbf{f} \quad (2)$$

$$\begin{aligned} \frac{\partial \rho(e + \mathbf{u} \cdot \mathbf{u}/2)}{\partial t} + \operatorname{div}(\rho(e + \mathbf{u} \cdot \mathbf{u}/2) \mathbf{u}) = \\ - \operatorname{div}(p \mathbf{u}) + \operatorname{div}(\bar{\bar{\tau}} \mathbf{u}) + \operatorname{div}(\lambda(\theta) \mathbf{grad} \theta) + \mathbf{f} \cdot \mathbf{u} + q \end{aligned} \quad (3)$$

where ρ is the density, p is the pressure, \mathbf{u} is the velocity, $\bar{\bar{\tau}}$ is the tensor of the viscous constraints, e is the internal energy, λ is the thermal conductivity, θ is

the temperature and \mathbf{f} is a general force term. In the case Newtonian fluids are considered, the tensor $\bar{\tau}$ can be written as:

$$\bar{\tau} = \mu(\theta) \left(\overline{grad\mathbf{u}} + {}^t \overline{grad\mathbf{u}} - \frac{2}{3} div(\mathbf{u}) \right) \quad (4)$$

where μ is the dynamic viscosity. Its value is calculated using the Sutherland's law as a function of temperature θ . q is a general source term for the energy equation. This system is closed using the equation of state for perfect gas $p = \rho r \theta$ where r is the specific gas constant.

2.2. Immersed Boundary Method for compressible flows: numerical formulation

The IBM proposed in this work roots in recent proposals by Riahi et al. [20] which was successfully used for the analysis of compressible flows around immersed bodies with adiabatic walls. The IBM strategy relies on communication between an Eulerian mesh used for calculation of the flow and Lagrangian markers representing the discretized shape of the immersed geometry. The communication between the two frames of reference allows for the calculation of the dynamic effects acting on the body surface in the Lagrangian space and for their representation on the Eulerian mesh as source terms.

The first step is the interpolation of physical quantities calculated on the Eulerian mesh to the Lagrangian markers. Lowcase type is used for information on the Eulerian setting, while capital letters (or via the subscript L for Greek letters) are used to indicate physical quantities on the Lagrangian markers. The interpolation operator \mathcal{I} used in this work is:

$$\mathcal{I}[\mathbf{p}]_{X_s} = [\mathbf{P}](X_s) = \sum_{j \in D_s} (\mathbf{p})_j^n \delta_h(\mathbf{x}_j - \mathbf{X}_s) \Delta \mathbf{x} \quad (5)$$

where \mathbf{p} and \mathbf{P} are a physical quantity, scalar or vectorial (θ or $\rho \mathbf{u}$ for example) and \mathbf{x} and \mathbf{X} represent the physical coordinates. For each Lagrangian marker s , D_s represents the set of points of the Eulerian mesh from which information is extracted (computational stencil) and the interpolation kernel δ_h

is the discretized delta function used in Pinelli et al. [21]:

$$\delta_h(r) = \begin{cases} \frac{1}{3}(1 + \sqrt{1 - 3r^2}) & 0 \leq r \leq 0.5 \\ \frac{1}{6}(5 - 3r - \sqrt{1 - 3(1 - r)^2}) & 0.5 \leq r \leq 1.5 \\ 0 & \text{otherwise} \end{cases} \quad (6)$$

$\Delta \mathbf{x}$ refers to an Eulerian quadrature, which is $\Delta \mathbf{x} = \Delta x \Delta y \Delta z$ for a Cartesian mesh with uniform distribution. This step is essential for the calculation of the dynamic effects on the immersed body surface. These effects, which will be detailed in section 2.2.1, are represented as source terms for both the momentum equation (\mathbf{F}) and the energy equation (Q).

The second step of the IBM procedure is the spreading of the volume force calculated in the first step to the Eulerian mesh elements. We will refer to this term as \mathbf{R} , knowing that the numerical procedure for \mathbf{F} and Q is the same. The value of the source term evaluated on the Eulerian mesh, $\mathbf{r}(\mathbf{x}_j)$, is given by:

$$\mathbf{r}(\mathbf{x}_j) = \sum_{k \in D_j} \mathbf{R}_k \delta_h(\mathbf{x}_j - \mathbf{X}_k) \epsilon_k \quad (7)$$

The k -index controls a loop over the Lagrangian markers whose support contains the Eulerian node j . ϵ_k is the Lagrangian quadrature, which is calculated by solving a linear system to satisfy a partition of unity condition. This system can be written in the form

$$A \epsilon = \mathbf{1} \quad (8)$$

where $\epsilon = (\epsilon_1, \dots, \epsilon_{N_s})^t$ $\mathbf{1} = (1, \dots, 1)^t$ are vectors whose size is equal to the number of Lagrangian markers N_s . On the other hand, the component A_{kl} of the matrix A is the product between the k^{th} and the l^{th} interpolation kernels:

$$A_{kl} = \sum_{j \in D_l} \delta_h(x_j - X_k) \delta_h(x_j - X_l) \quad (9)$$

The calculation of the dynamic effects associated with the presence of the immersed body in step one is thus crucial for obtaining a precise representation

of the flow. The research team [20] was able to derive an expression for the source term of the momentum equation \mathbf{F} which takes into account the iterative nature of numerical solvers used for the calculation:

$$\mathbf{F} = a_s \left((\rho_L \mathbf{U})^d - \overline{(\rho_L \mathbf{U})} \right) \quad (10)$$

where a_s is a coefficient derived by the discretization procedure. The superscript d over the physical quantities represents the target behavior of the flow (i.e. zero velocity at the wall) while the overbar represents the result of the interpolation of the quantities from the Eulerian mesh performed in step one.

The novelty of the present approach is represented by the inclusion of a volume source term q for the energy equation, which mimics heat transfer phenomena on the body surface. These effects are derived from the discretized set of equations via analytic manipulation. In the present analysis, the heat transfer will be considered equivalent to a boundary condition applied on the surface of the immersed body. The analysis will be restricted to the case of *imposed temperature at the wall*, which is equivalent to imposing a Dirichlet condition for the temperature field.

2.2.1. Imposed temperature on the body surface - analytic derivation

Similarly to previous works [9, 20], the starting point is represented by the discretized set of equation in the Eulerian frame of reference for the mesh element of coordinate x . Time advancement from the instant n to $n + 1$ is considered. For sake of simplicity, the procedure for the momentum equation and the forcing \mathbf{F} (detailed in [20]) is not reported here, and the development is provided only for the internal energy equation 3. Its discretized form for an iterative solver can be written as:

$$a_e (\rho e)^{n+1} = \phi_e^{n+1/2} + f_e^{n+1/2} + q_e^{n+1/2} \quad (11)$$

with:

- a_e : coefficient derived by the discretization procedure

- ϕ_e : discretization term calculated at the intermediate time $n + \frac{1}{2}$ which includes the contribution of the convection term, the heat flux, the pressure work and the viscous friction work.
- $f_e^{n+1/2}$: discretized form of the term $\mathbf{f} \cdot \mathbf{u}$
- $q_e^{n+1/2}$: discretization of the volume source term q . This term represents the heat exchange between the flow and the immersed body, calculated at the intermediate time $n + \frac{1}{2}$

One must keep in mind that \mathbf{f} represent the discretized volume source term representing the effect of the body in the momentum equation, as in classical IBM strategies. Thus, the term q_e is its correspondent in the energy equation, which describes the heat transfer between the flow and the immersed body. Thus, if one targets a behavior of the internal energy $(\rho e)^d$ at the instant $n + 1$, then the optimized value of the volume source term q_e must comply with the equation:

$$q_e^{n+1/2} = a_e (\rho e)^d - \phi_e^{n+1/2} - f_e^{n+1/2} \quad (12)$$

By applying the Eulerian-Lagrangian transformation via the interpolation operator proposed by Pinelli et al.[21], the equation 12 on the Lagrangian markers representing the body surface in the IBM method is transformed in:

$$Q_e^{n+1/2} = a_e (\rho_L E)^d - \Phi_e^{n+1/2} - F_e^{n+1/2} \quad (13)$$

- $(\rho_L E)^d$: target internal energy value on the Lagrangian markers
- $\Phi_e^{n+1/2}$: total contribution of the convection term, the pressure work term, the viscous friction work term and heat flux term interpolated on the Lagrangian marker at the time $n + \frac{1}{2}$

Let us now consider again equation 11 in the case of the presence of the body surface does not introduce direct thermal interactions with the flow. This state will be referred to as neutral behavior. In this case, the time advancement to $n + 1$ (a suffix l is here used) reads as:

$$a_e (\rho e)^l = \phi_e^{n+1/2} + f_e^{n+1/2} \quad (14)$$

If one further performs a transformation from the Eulerian system to the Lagrangian frame of reference, equation 14 becomes:

$$a_e (\rho_L E)^l = \Phi_e^{n+1/2} + F_e^{n+1/2} \quad (15)$$

where $(\rho_L E)^l$ represents the internal energy at a Lagrangian point X_s .

Combining the two equations 13 et 15, an analytic expression for the volume source term for the energy equation to be included in the IBM method is derived:

$$Q_e^{n+1/2} = a_e ((\rho_L E)^d - (\rho_L E)^l) \quad (16)$$

Equation 16 can be further manipulated if one considers that $e = c_v \theta$ for a perfect gas. Therefore, the volume source term for the internal energy equation can be written as a function of the temperature:

$$Q_e^{n+1/2} = a_e c_v ((\rho_L \Theta)^d - (\rho_L \Theta)^l) \quad (17)$$

with

- c_v : the thermal capacity at constant volume of the interpolated fluid at Lagrangian markers
- $(\rho_L \Theta)^d$: the desired temperature density at the Lagrangian markers
- $(\rho_L \Theta)^l$: interpolated temperature density at the Lagrangian markers for a neutral system.

A choice relying on numerical arguments has also been performed for the term $\mathbf{f} \cdot \mathbf{u}$ in the energy equation, which has been systematically set to zero. This term is naturally zero when the body is still, but it shows non-zero values in the case of body movement. However, this term is always very small so interpolation errors are most of the time larger in magnitude, leading to numerical instability and degradation of the accuracy. We therefore decided to remove it from the energy equation.

2.2.2. IBM implementation in OpenFOAM numerical solvers

The implementation of the IBM algorithm has been performed in the open source library OpenFOAM, owing to previous development of the research group [19, 20]. Two solvers for compressible flows have been considered: *sonicFoam* and *rhoCentralFoam*. These two solvers are studied to provide optimal performance for different ranges of Ma numbers. The main features of the solvers are discussed in [20]. The newly generated solvers will be referred to in the following as *IBM-HT* versions of the initial solver modified and are now presented. One must consider that the versions of the solvers proposed in [20] are *neutral* with respect to the heat transfer behavior i.e. the presence of the body surface is transparent with respect to heat exchange. Details about the algorithmic structure of *IBM-HT-sonicFoam* and *IBM-HT-rhoCentralFoam* are provided in Appendix A and Appendix B, respectively.

For every test case investigated with these solvers, the numerical discretization used for the gradient and divergence operators in the dynamic equations is linear (i.e. second order centered schemes). A van Leer limiter, which improves the flow prediction in the regions where shocks are observed, is used for the flux interpolation. Also, a grid convergence study is provided in Appendix C

3. Numerical validation of the *IBM-HT* algorithms

Validation of the new solvers is performed on the 2D flow around a heated circular cylinder. This classical test case has been extensively investigated in the literature for a large spectrum of values of Re , Ma and temperature ratio $r_\theta = \frac{\theta_{wall}}{\theta_{inlet}}$, where θ_{wall} is the wall temperature of the immersed body and θ_{inlet} is the temperature imposed at the inlet. Numerous databases are available for comparison.

3.1. Test case - numerical details

The center of the cylinder is the origin of the domain in $(0, 0)$ and its diameter is equal to D . The dimensions of the computational domain are

$[-16D, 48D] \times [-16D, 16D]$ in the streamwise direction (x) and normal direction (y), respectively. The mesh elements are uniformly distributed in the central zone near to cylinder $x \times y \in [-D, D] \times [-D, D]$. Their size is equal to $\Delta x = \Delta y = 0.01D$. Outside this region, the mesh is progressively coarsened moving through five different levels as shown in Figure 1. The passage from one level to another implies a coarsening ratio of the elements of 2 in both x and y directions. This value is smoothed in correspondence of the boundaries of the refinement regions. This transition in the mesh is generated via an OpenFOAM native tool, *snappyHexMesh*, and the Finite Volume discretization used in the solvers suitably takes it into account. In fact, the solver imposes conservation of the fluxes through the faces of the mesh elements, granting conservativity of the Navier–Stokes equation even with abrupt changes in the resolution of the mesh. Nonetheless, we have paid attention that these transition regions do not occur near the Eulerian supports for each Lagrangian Marker, for this test case and all the other flow configurations presented in the following Sections. This task has been easy to perform as it is connected with the need to impose a refined mesh distribution in the vicinity of the immersed body. The total number of mesh elements that result is equal to 1.5×10^5 . The positioning of the Lagrangian markers is performed so that each Eulerian mesh element crossed by the body surface includes at least one marker. This strategy has been performed as the original version of the method has shown sensitivity to *holes* in the connection between the Eulerian and the Lagrangian space [21]. The IBM library integrates an internal check routine which keeps only the Lagrangian marker closer to the center of each mesh element, if one or more markers are detected. For the mesh previously introduced, 401 Lagrangian markers have been used.

The boundary conditions have been chosen accordingly to general guidelines in the literature and using the team’s experience for each of the Ma number investigated, selecting different options for subsonic and supersonic flows. More precisely, a constant velocity inlet condition is imposed upstream (left side), a mass conserving outlet condition is prescribed downstream and slip (subsonic)

or non reflective (supersonic) conditions are imposed in the normal direction.

For each case analyzed, a number of different coefficients are compared with available data of the literature. Aerodynamic forces are determined via the bulk flow coefficients known as drag coefficient C_d and lift coefficient C_l :

$$C_d = \frac{2F_x}{\rho_\infty U_\infty^2}, \quad C_l = \frac{2F_y}{\rho_\infty U_\infty^2} \quad (18)$$

the forces in the streamwise direction F_x and in the normal F_y are directly calculated on the Lagrangian markers. ρ_∞ and U_∞ indicate asymptotic physical quantities imposed at the inlet.

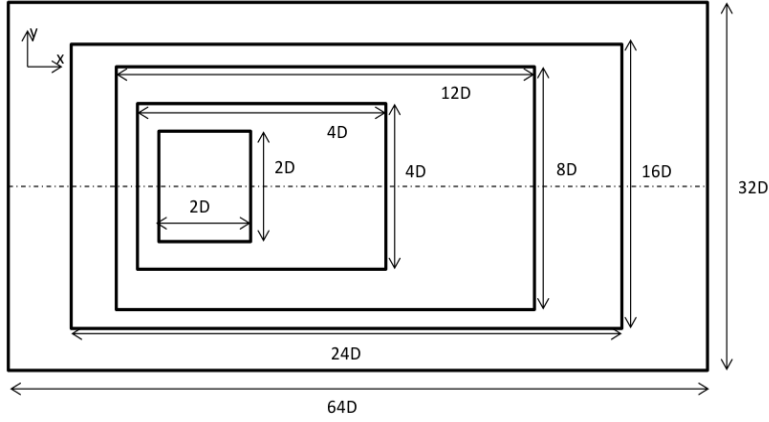


Figure 1: 2D computational domain used for *IBM-HT* validation.

3.2. Unsteady flow around a heated 2D circular cylinder

The flow around a heated circular cylinder in unsteady regime is now investigated to further assess the performance of the source term for the internal energy equation. The non-dimensional parameters are set to $Ma = 0.01$ using temperature ratio $r_\theta = 1.8$ and three Reynolds number $Re = \{100, 140, 260\}$. For these cases, variations in the temperature field significantly influence the flow organization, especially when the temperature ratio r_θ is larger than 1.1 [22].

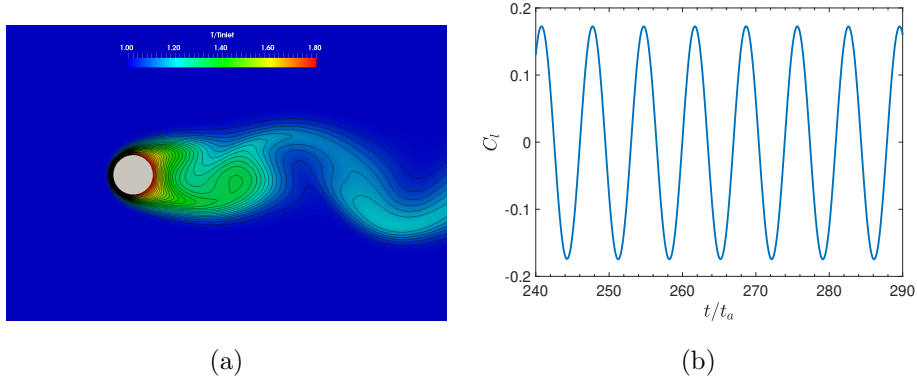


Figure 2: Isocontours of the temperature (a) and time evolution of the lift coefficient (b) for the flow past a circular cylinder for $Ma = 0.01$, $Re = 100$ and $r_\theta = 1.8$. $t_a = D/U_\infty$ is the characteristic advection time.

For the different cases, an unsteady behavior characterized by a periodic von Kármán wake is observed. Qualitative visualizations of the instantaneous regimes are shown with the temperature isocontours in Figure 2 (a). In addition the time evolution of the lift coefficient is shown in Figure 2 (b).

One important parameter describing the flow is the Strouhal number $S_t = \frac{fD}{U_\infty}$, where f is the shedding frequency computed using the time evolution of the lift coefficient C_l . Comparison shows a good agreement with results available in the literature [22, 23], see Figure 3. We observe that the vortex shedding frequency, f , and thus the Strouhal number S_t , increases for increasing values of Re for a given r_θ . Finally, in table 1 the computed bulk flow quantities for the flow for all values of Re are reported. It can be seen that the average value of the drag coefficient C_d decreases when Re increases. On the other hand, the maximum value of the coefficient of lift C_l^{max} exhibits the opposite variation, increasing with Re . These results are in agreement with the findings by Homsy et al. [24].

4. Forced convection from an heated sphere in a steady regime

The three-dimensional flow around a sphere is now investigated. This test case, which is significantly more complex, allows for a robust validation of the

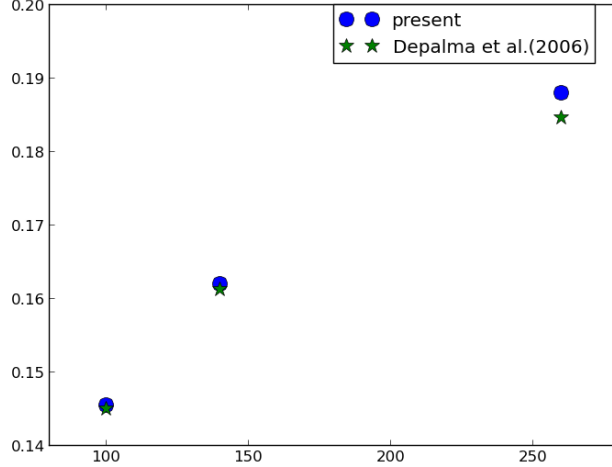


Figure 3: Strouhal number versus Reynolds number for flow past a heated cylinder: comparison between present results and literature data

Present study - $\mathbf{r}_\theta = 1.8$	C_d	C_l^{max}
$Re = 100$	1.48	0.18
$Re = 140$	1.46	0.29
$Re = 260$	1.45	0.53

Table 1: C_d and C_l^{max} for unsteady flow around heated circular cylinder at $Ma = 0.01$.

capability of the IBM method to accurately capture heat exchange.

4.1. Numerical and computational ingredients

The computational domain is here set to $x \times y \times z = [-16D, 48D] \times [-16D, 16D] \times [-16D, 16D]$ where D is the diameter of the sphere. Again, the center of the body is set in the origin of the system and the mesh is obtained using the tool *snappyHexMesh*. The mesh is made by hexahedral uniform elements which are progressively refined approaching the sphere region (see figure 4). The size of the elements is refined by a factor two in each space direction when crossing the prescribed interfaces between regions at dif-

ferent resolution. The central most refined region is defined by the coordinates $x \times y \times z = [-1.25D, 1.25D] \times [-1.25D, 1.25D] \times [-1.25D, 1.25D]$. Within this region, the mesh resolution is $\Delta x = \Delta y = \Delta z = 1/64D$. This mesh is composed by a total of 5×10^6 elements and was already used for analysis of compressible flows [20]. The choice of the number and positioning of the Lagrangian markers follows the same strategy presented for the flow around a circular cylinder discussed in sec. 3.1. Here 12119 Lagrangian markers are used.

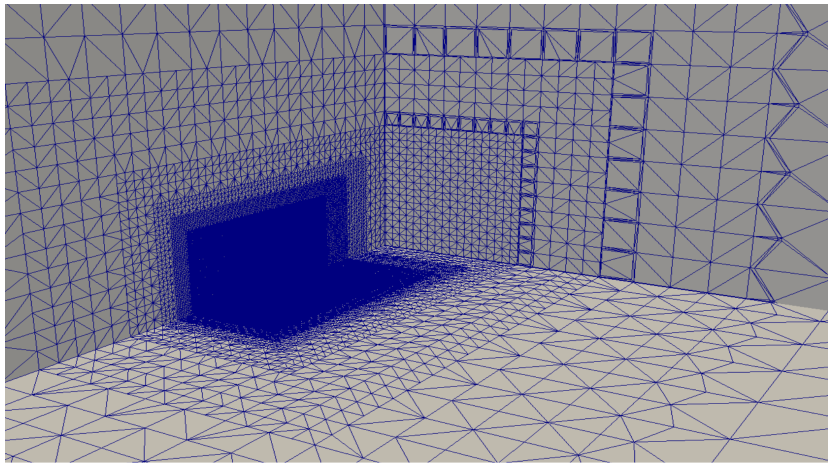


Figure 4: Visualization of cutting planes inside the 3D mesh used for the calculation of the flow around a sphere.

In order to provide a suitable representation of the physical features of the flow, the *IBM-HT-rhoCentralFoam* solver is employed for this study.

4.2. Physical regimes observed for several r_θ

This test case has been chosen because of the emergence of different regimes which exhibit a very high sensitivity to the values of temperature ratio $r_\theta = 1.1, 1.5, 2$, representing a challenging test case of validation. We choose to investigate heated flow around sphere at $Ma = 0.8$ and $Re = 300$ and the isocontours of the velocity field (represented in terms of Ma) and the temperature are shown in Figure 5 for the three cases. One can see that the flow undergoes a transition from an unsteady regime to a steady axisymmetric state. This effect

is clearly driven by the heat exchange dynamics. Results are compared with recent data reported in the literature for body-fitted numerical simulations using high order discretization schemes [25] (Table 2). The physical quantities compared are the mean drag coefficient $\overline{C_d}$, the length of the recirculation bubble l_s and the Strouhal number St . One can see that a reasonably good agreement is obtained, and in particular variations with different r_θ values are very similar. It appears that the IBM tends to provide a slight over prediction (around 10%) of the mean drag coefficient $\overline{C_d}$ when compared with body-fitted simulations. This result, which was already observed in previous studies [20], is probably associated with mesh resolution and the numerical schemes employed for the analysis.

	Studies	$\overline{C_d}$	l_s	St
Ma=0.8	Present ($r_\theta = 1.1$)	0.895	2.9	0.104
Re=300	Nagata [25] (Num.)	0.81	2.8	0.105
	Present ($r_\theta = 1.5$)	0.93	3.18	
	Nagata [25] (Num.)	0.85	3.1	
	Present ($r_\theta = 2$)	0.99	3.4	
	Nagata [25] (Num.)	0.91	3.35	

Table 2: Bulk flow quantities for the flow past a sphere obtained via IBM simulation. Present results are compared with available data in the literature. $\overline{C_d}$ is the mean, time-averaged drag coefficient, l_s is the recirculation length and St is the Strouhal number.

4.3. Investigation of the supersonic flow around a sphere

The supersonic flow for $Ma = 2$, $Re = 300$ and $r_\theta = 2$ is now investigated, using the same mesh previously employed. In this case compressibility effects are very strong and a steady axisymmetric configuration is observed, as qualitatively shown in figure 6. The main bulk flow quantities are again compared with results obtained from body-fitted numerical simulations [25] and reported in table 3. It appears that all the physical features are in agreement with the data in the literature [25], assessing the potential of the IBM method developed. A

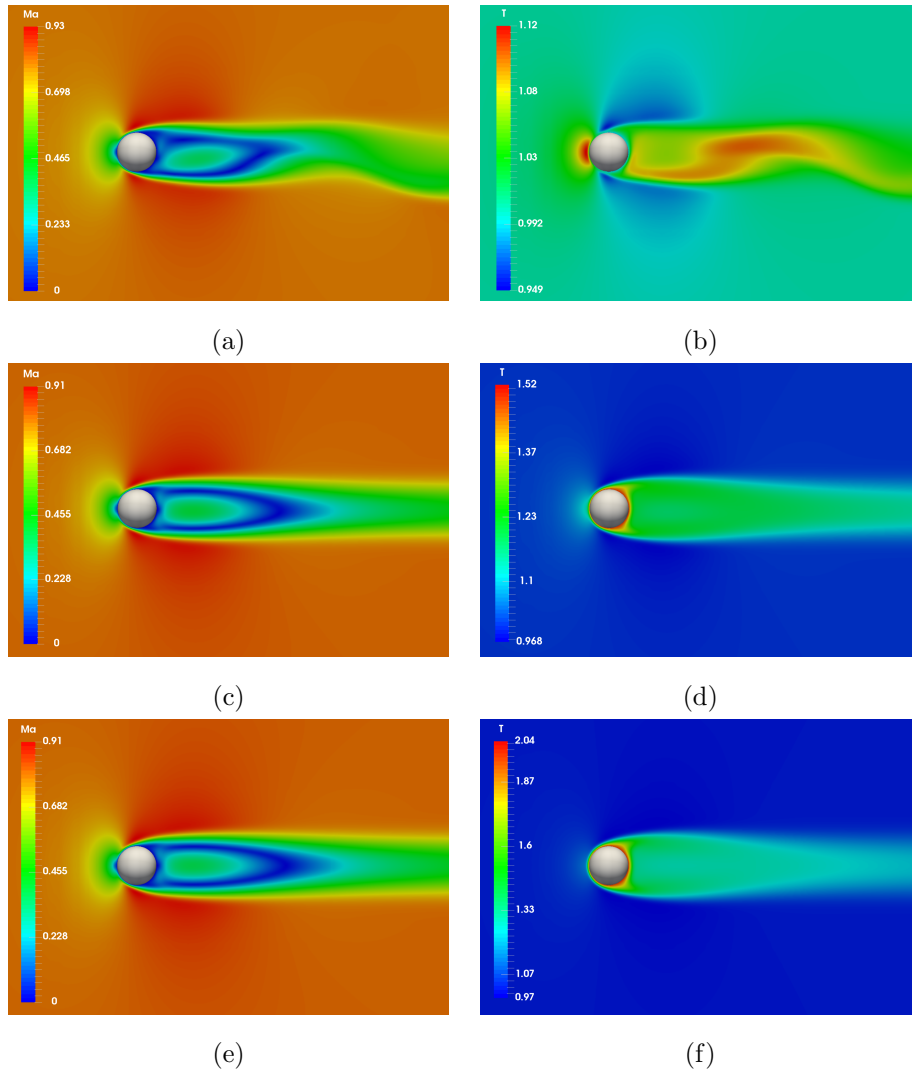


Figure 5: Iso-contours of Ma number and temperature for $Ma = 0.8$ and $Re = 300$: (a) $r_\theta = 1.1$; (b) $r_\theta = 1.5$; (c) $r_\theta = 2$

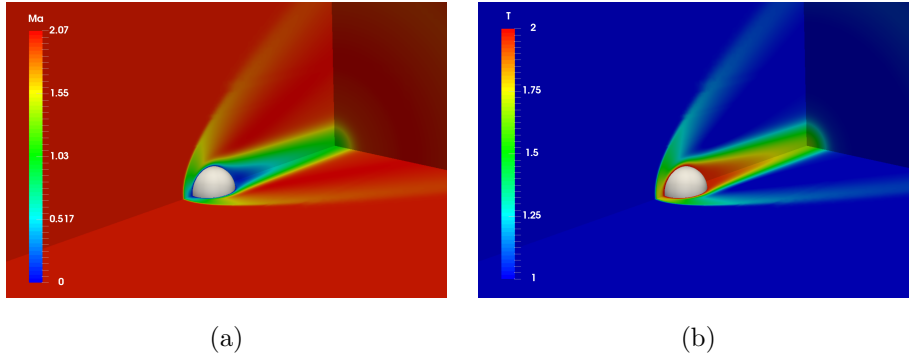


Figure 6: Numerical simulation of the supersonic flow around a sphere for $Ma = 2$, $Re = 300$ and $r_\theta = 2$: (a) Isocontours of the Ma number (b) isocontours of the Temperature

slight over prediction (this time around 5%) of the drag coefficient C_D is again observed, while the recirculation length l_s and the distance of the shock from the wall Δ_{shock} are very similar.

	Studies	$\overline{C_d}$	l_s	Δ_{shock}
Ma=2	Present ($r_\theta = 2$)	1.48	0.85	0.23
Re=300	Nagata [25] (Num.)	1.41	0.85	0.25

Table 3: Bulk flow quantities for the flow past a sphere obtained via IBM simulation. Present results are compared with available data in the literature. C_d is the time-averaged drag coefficient, x_s is the recirculation length, Nu Nusselt number and D_{shock} is the shock distance.

5. Fluid - Structure interaction : oscillating cylinder with fixed wall temperature

In this last section, the flow around an oscillating two-dimensional cylinder is investigated. The simulation is performed using the *IBM - HT - rhoCentralFoam* solver.

The motion of the cylinder is imposed in the streamwise direction x , providing an explicit law of movement for the Lagrangian markers following a sinus law. More precisely, the position in the streamwise direction of the Lagrangian

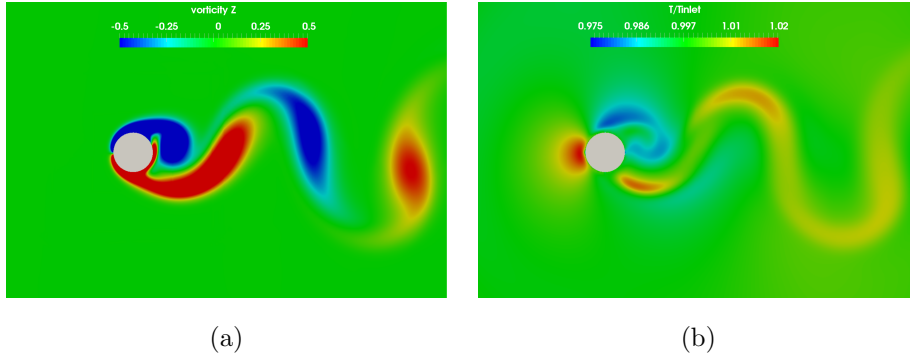


Figure 7: Iso-contours vorticity (a) and temperature (b) for the flow around a longitudinal oscillating cylinder $Re = 100$, $r_\theta = 1$

markers is updated in time following the equation:

$$X_s(t) = X_s(0) + A \sin(2\pi f_c t) \quad (19)$$

with $A = 0.14 \times D$ and $f_c = 2 \times f_0$. A preliminary calculation is performed on a fixed cylinder to determine the shedding frequency f_0 . The values of the parameters have been chosen in order to allow comparison with a study proposed by Luo et al. [26] with $Ma = 0.3$, $Re = 100$ and $r_\theta = 1$. In figure 7 the qualitative evolution of the isocontours of the temperature and of the vorticity are shown after the initial transient. The comparison of present results with the findings by Luo et al. [26] in terms of the time evolution of the drag coefficient C_d and lift coefficient C_l is very good, as shown in figure 8. Therefore, the *IBM-HT* model has proven good accuracy even for a more complex case including fluid-structure interaction.

An additional simulation with imposed temperature $r_\theta = 2$ was carried out in order to study the effects of the increase in temperature on the aerodynamic parameters 9. The variation in temperature affects the viscosity close to the wall, which modifies the aerodynamic performance. The comparison of the drag coefficient C_d and lift coefficient C_l for the two cases, which are shown in fig. 10, shows important differences. In particular, the maximum value of C_l decreases for the case with $r_\theta = 2$, in agreement with the findings by Homsy et al. [24].

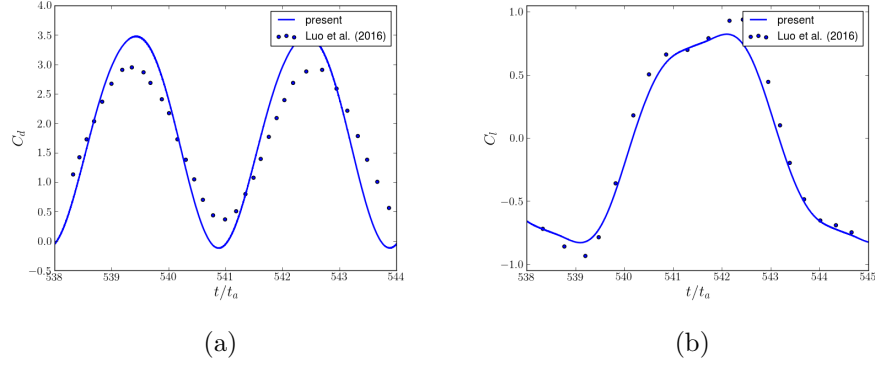


Figure 8: Comparison of the (a) drag coefficient C_d and (b) lift coefficient C_l for the flow around a longitudinal oscillating cylinder, $r_\theta = 1$ with results by Luo et al. [26]

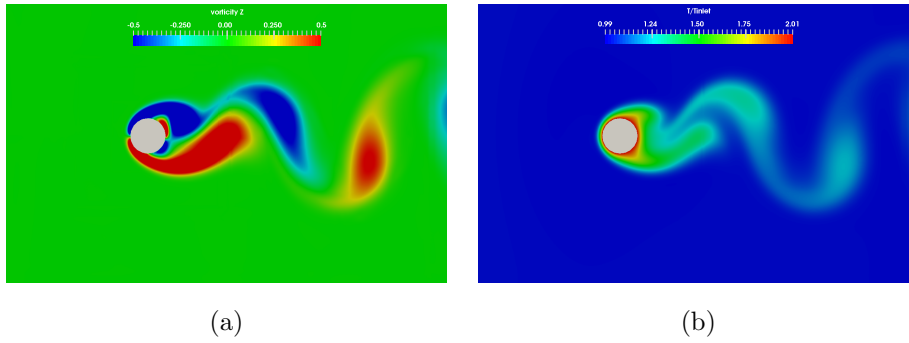


Figure 9: Iso-contours vorticity (a) and temperature (b) for a flow around a longitudinal oscillating cylinder with $r_\theta = 2$

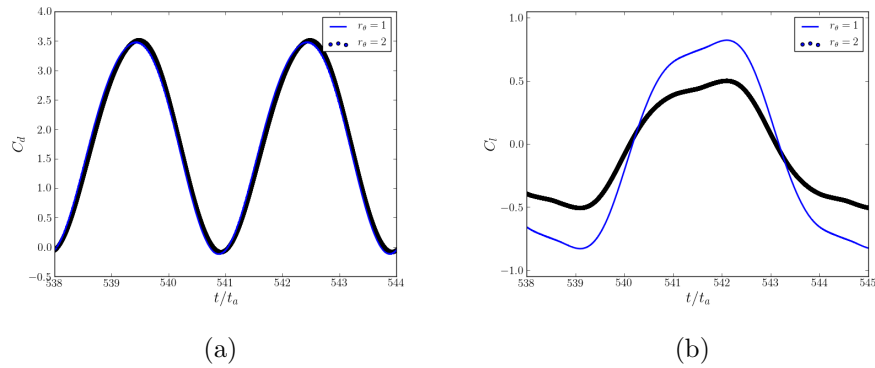


Figure 10: (a) Temporal evolution of the drag coefficient C_d and (b) of the lift coefficient C_l for flow around an oscillating circular cylinder. The cases for $r_\theta = 1$ and $r_\theta = 2$ are compared

6. Conclusion

In this paper, a discrete-forcing immersed boundary method was proposed for simulating both heat exchange and compressible flows, for stationary and moving bodies. The proposed methodology introduces an additional heat source term to the right hand side of the energy equation to keep the solid boundary at the prescribed temperature. The compressible Navier-Stokes equations are discretized on a Cartesian grid and solved by either the `sonicFoam` or the `rhoCentralFoam` solver of the `OpenFOAM` platform according to the Mach number of the flow.

To validate the robustness and accuracy of the proposed method, a series of simulations was performed on canonical forced convection flows with comparison with existing results. Both the flow dynamics and the heat transfer were in good agreement with the data in literature. The 3D flows around an isothermal sphere in the transonic and supersonic regimes were investigated. Different wall temperature conditions were applied leading to the transition between an unsteady periodical wake and a steady axisymmetric state. The results obtained with the proposed method were found in close agreement with recent direct numerical simulations available in the literature, demonstrating the capability of the numerical strategy to treat both compressible and heated flows with satisfactory accuracy. Finally the method was successfully validated on a benchmark case involving moving boundaries, for which the computational cost of remeshing techniques would be significantly high for classical body-fitted approaches. Future works envision an improvement in accuracy for higher Reynolds number configurations, including wall modelling within the formulation of the IBM model.

Acknowledgement

The research work has been developed using computational resources within the framework of the project gen7590-A0012A07590 DARI-GENCI.

References

- [1] C.S. Peskin. Flow patterns around heart valves: a numerical method. *Journal of Computational Physics*, 10:252–271, 1972.
- [2] C.S. Peskin. The immersed boundary method. *Acta Numerica*, 11:479–517, 2002.
- [3] R. Mittal and G. Iaccarino. Immersed boundary methods. *Annual Review of Fluid Mechanics*, 37:239–261, 2005.
- [4] X. Yang and F. Sotiropoulos. Immersed boundary methods for simulating fluid-structure interaction. *Progress in Aerospace Sciences*, 65:1–21, 2014.
- [5] W. Kim and H. Choi. Immersed boundary methods for fluid-structure interaction: a review. *International Journal of Heat and Fluid Flow*, 75:301–309, 2019.
- [6] R.P. Beyer and R.J. Leveque. Analysis of a one-dimensional model for the immersed boundary method. *SIAM Journal on Numerical Analysis*, 29:332–364, 1992.
- [7] D. Goldstein, R. Handler, and L.F. Sirovich. Modeling a no-slip flow with an external force field. *Journal of Computational Physics*, 105:354–366, 1993.
- [8] E.A. Fadlun, R. Verzicco, P. Orlandi, and J. Mohd-Yusof. Combined immersed-boundary finite-difference methods for three-dimensional complex flow simulations. *Journal of Computational Physics*, 161:35–60, 2000.
- [9] M. Uhlmann. An immersed boundary method with direct forcing for the simulation of particulate flows. *Journal of Computational Physics*, 209:448–476, 2005.
- [10] Y. Cheny and O. Botella. The ls-stag method: A new immersed boundary/level-set method for the computation of incompressible viscous

- flows in complex moving geometries with good conservation properties. *Journal of Computational Physics*, 229:1043–1076, 2010.
- [11] V. Kumar, A. Sharma, and R.K. Singh. Central upwind scheme based immersed boundary method for compressible flows around complex geometries. *Computers and Fluids*, 196:104349, 2020.
- [12] J. Kim, D. Kim, and H. Choi. An immersed-boundary finite-volume method for simulations of flow in complex geometries. *Journal of Computational Physics*, 171:132–150, 2001.
- [13] W. Ren, C. Shu, and W. Yang. An efficient immersed boundary method for thermal flow problems with heat flux boundary conditions. *International Journal of Heat and Mass Transfer*, 64:694–705, 2013.
- [14] S. G. Park, C. B. Chang, B. Kim, and H.J. Sung. Simulation of fluid-flexible body interaction with heat transfer. *International Journal of Heat and Mass Transfer*, 110:20–33, 2017.
- [15] K. Luo, Z. Zhuang, J. Fan, and N.E.L. Haugen. A ghost-cell immersed boundary method for simulations of heat transfer in compressible flows under different boundary conditions. *International Journal of Heat and Mass Transfer*, 92:708–717, 2015.
- [16] K. Luo, C. Mao, Z. Zhuang, J. Fan, and N.E.L. Haugen. A ghost-cell immersed boundary method for the simulations of heat transfer in compressible flows under different boundary conditions part-ii: Complex geometries. *International Journal of Heat and Mass Transfer*, 104:98–111, 2016.
- [17] Y. Qu, R. Shi, and R.C. Batra. An immersed boundary formulation for simulating high-speed compressible viscous flows with moving solids. *Journal of Computational Physics*, 354:672–691, 2018.
- [18] E. Khalili, M. Larsson, and B. Muller. Immersed boundary method for viscous compressible flows around moving bodies. *Computers and Fluids*, 170:77–92, 2018.

- [19] E. Constant, J. Favier, M. Meldi, P. Meliga, and E. Serre. An immersed boundary method in openfoam : verification and validation. *Computers & Fluids*, 157:55–72, 2017.
- [20] H. Riahi, M. Meldi, J. Favier, E. Serre, and E. Goncalves. A pressure-corrected immersed boundary method for the numerical simulation of compressible flows. *Journal of Computational Physics*, 2018.
- [21] A. Pinelli, I. Naqavi, U. Piomelli, and J. Favier. Immersed-boundary methods for general finite-difference and finite-volume navier–stokes solvers. *Journal of Computational Physics*, 229:9073–9091, 2010.
- [22] P. De Palma, M.D. de Tullio, G. Pascazio, and M. Napolitano. An immersed-boundary method for compressible viscous flows. *Computers and Fluids*, 35:693–702, 2006.
- [23] M.D. de Tullio, P. De Palma, G. Iaccarino, G. Pascazio, and M. Napolitano. An immersed boundary method for compressible flows using local grid refinement. *Journal of Computational Physics*, 225:2098–2117, 2007.
- [24] R. Homsy, MD D. Islam, Y.Y. Fatt, and I. Janajreh. Flow dynamics over a heated cylinder subjected to high temperature ratios. *Case Studies in Thermal Engineering*, 27:101357, 2021.
- [25] T. Nagata, T. Nonomura, S. Takahashi, Y. Mizuno, and K. Fukuda. Direct numerical simulation of flow around a heated/cooled isolated sphere up to a reynolds number of 300 under subsonic to supersonic conditions. *International Journal of Heat and Mass Transfer*, 120:284–299, 2018.
- [26] K. Luo et al. A ghost-cell immersed boundary method for simulations of heat transfer in compressible flows under different boundary conditions. *International Journal of Heat and Mass Transfer*, 92:708–717, 2016.

Appendix A. IBM-HT-sonicFoam

The complete algorithm with integration of the IBM method can be summarized in the following steps:

1. The discretized continuity, momentum and energy equations are resolved, providing a first time advancement of ρ^* , \mathbf{u}^* and θ^* . These quantities are calculated imposing $\mathbf{f} = 0$ and $q = 0$.
2. The fields calculated in step 1 are *interpolated* on the Lagrangian markers in order to obtain the value of the forcing \mathbf{F} and the source term Q . These quantities are *spread* over the Eulerian mesh, in order to provide the contributions for \mathbf{f} and q in each Eulerian mesh element.
3. The whole system is resolved again, starting from stored quantities for the time step n and but now including the source terms previously calculated for the momentum equation and the internal energy equation. An iterative procedure is triggered until convergence:

$$\rho^{n+1} = \frac{\phi_\rho(\rho^*, \mathbf{u}^*)}{a_\rho} \quad (\text{A.1})$$

$$\mathbf{u}^{n+1} = \frac{\phi_\mathbf{u}(\rho^{n+1}, \mathbf{u}^*)}{a_\mathbf{u}} - \frac{\mathbf{grad}p^*}{a_\mathbf{u}} + \frac{\mathbf{f}}{a_\mathbf{u}} \quad (\text{A.2})$$

$$e^{n+1} = \frac{\phi_e(\rho^{n+1}, \mathbf{u}^{n+1}, e^*)}{a_e} - \frac{\text{div}(p^* \mathbf{u}^{n+1})}{a_e} + \frac{q}{a_e} \quad (\text{A.3})$$

$$p^{n+1} = \frac{\phi_p(p^*, \rho^{n+1}, \mathbf{u}^{n+1})}{a_p} + \frac{\phi_{fp}(\mathbf{f})}{a_p} \quad (\text{A.4})$$

In this case, the terms \mathbf{f} and q are not updated during the step 3. They are calculated only once in step 2.

Appendix B. IBM-HT-rhoCentralFoam

The integration of the *IBM-HT* method in the solver rhoCentralFoam presented in [20] follows these steps:

1. A prediction step resolving continuity, momentum and energy equations is performed in order to obtain first estimations for ρ^* , e^* and \mathbf{u}^* (and p^* via an equation of state). The volume sources are here $\mathbf{f} = \mathbf{0}$ and $q = 0$.
2. The physical quantities ρ^* , p^* , e^* and \mathbf{u}^* are interpolated in the Lagrangian space and \mathbf{F} and Q are calculated. This field is *spread* over to the Eulerian mesh, so that the value of the forcing terms \mathbf{f} and q for each mesh cell is calculated.
3. Equations of the first step are resolved again including the IBM forcing:

$$\rho^{n+1} = \frac{\phi_\rho(\rho^*, \mathbf{u}^*)}{a_\rho} \quad (\text{B.1})$$

$$(\rho\mathbf{u})^{**} = \frac{\phi'_u((\rho\mathbf{u})^*)}{a_u} - \frac{\mathbf{grad}p^*}{a_u} \quad (\text{B.2})$$

$$(\mathbf{u})^{**} = (\rho\mathbf{u})^{**}/\rho^{n+1} \quad (\text{B.3})$$

$$\rho^{n+1}\mathbf{u}^{n+1} = \rho^{n+1}\mathbf{u}^{**} + \frac{\phi_u(\rho^*, \mathbf{u}^*)}{a_u} - \frac{\phi'_u((\rho\mathbf{u})^*)}{a_u} + \frac{\mathbf{f}}{a_u} \quad (\text{B.4})$$

$$(\rho e_t)^{**} = \frac{\phi'_{e_t}((\rho e_t)^*, \mathbf{u}^{**})}{a_{e_t}} - \frac{\text{div}(p^*\mathbf{u}^*)}{a_{e_t}} \quad (\text{B.5})$$

$$e^{**} = (\rho e_t)^{**}/\rho^{n+1} - 0.5((\mathbf{u})^{**} \cdot (\mathbf{u})^{**}) \quad (\text{B.6})$$

$$\theta^{**} = e^{**}/c_v \quad (\text{B.7})$$

$$\begin{aligned} \rho^{n+1}e^{n+1} &= \rho^{n+1}e^{**} + \frac{\phi_e(\rho^{n+1}, \mathbf{u}^{n+1}, e^n)}{a_e} - \frac{\text{div}(\lambda(\theta^{**})\mathbf{grad}(\theta^{**}))}{a_e} \\ &- \frac{\phi'_{e_t}((\rho e_t)^*, \mathbf{u}^{**})}{a_{e_t}} + \frac{q}{a_e} \end{aligned} \quad (\text{B.8})$$

4. Finally, the temperature $\theta^{n+1} = e^{n+1}/C_v$ and the pressure $p^{n+1} = \rho^{n+1} \cdot (r\theta^{n+1})$ are updated.

Appendix C. Grid convergence analysis

The accuracy of the proposed IBM method is assessed via the analysis of the flow around a circular cylinder for $Ma = 2.5$ and $Re = 250$. No heat exchange is considered in this validation.

A grid convergence analysis is performed evaluating results using four different grids. The mesh resolution in the near cylinder region is imposed to be $\Delta x = \Delta y = \left\{ \frac{D}{10}; \frac{D}{15}; \frac{D}{25}; \frac{D}{50} \right\}$ where D is the diameter of the cylinder. The

corresponding number of Lagrangian markers employed is $\{28; 39; 62; 104\}$, respectively. Data from the most refined mesh is used as a reference solution.

The precision of the IBM method is investigated using L_∞ norms so that, for a physical quantity ϕ , the error is estimated as:

$$e_{\phi L_\infty} = \|\phi_{ref} - \phi_G\|_\infty \quad (C.1)$$

where ϕ_G is the reference solution.

The behavior of error in the prediction of the drag coefficient C_D is shown in Figure C.11. In the framework of this IBM method, the drag coefficient is directly calculated using information available on the Lagrangian markers. For this quantity, the rate of convergence is almost 2.

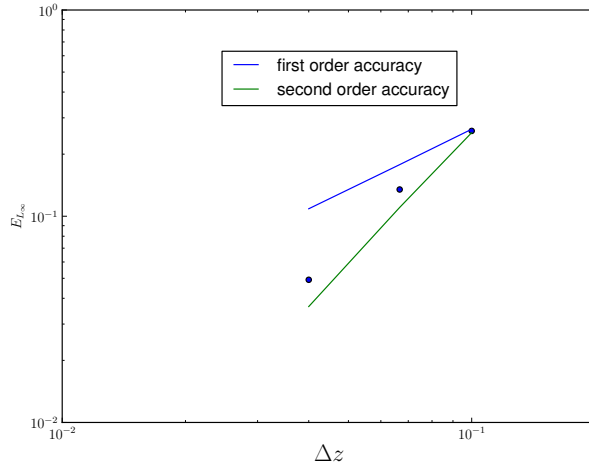


Figure C.11: Convergence rate in the prediction of the drag coefficient C_D using the IBM method presented in this work.

In addition, the qualitative evolution of the isocontours of the Mach number is presented in fig. C.12 for the coarsest and the finest mesh resolution. Despite the main flow features are captured by both simulations, one can see differences in the precision in particular close to the shock region, which is expected. The distribution of pressure coefficient $C_p = 2(p - p_\infty) / (\rho_\infty U_\infty^2)$ around the cylinder, which are shown in fig. C.13 against the azimuthal angle α , allow to draw the

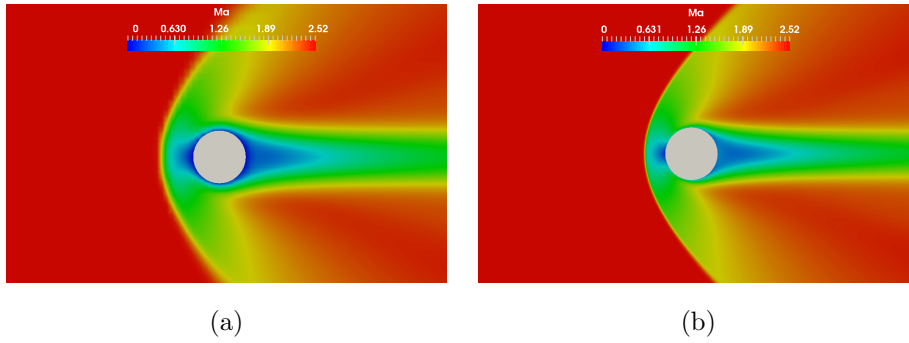


Figure C.12: Isocontours of Ma number : (a) $\Delta x = \Delta y = 0.1$ and (b) $\Delta x = \Delta y = 0.02$

same conclusions. The qualitative behavior of the coarsest and finest simulation is very similar, but differences can be observed in particular for the stagnation point for $\alpha = 0$.

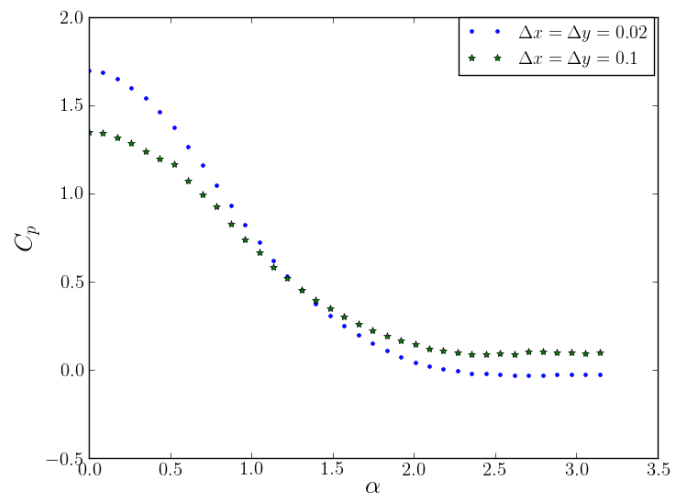


Figure C.13: Pressure coefficient distributions for the cases $\Delta x = \Delta y = 0.1$ and $\Delta x = \Delta y = 0.02$